Signature of Tetrahedral Ge in the Raman Spectrum of Amorphous Phase-Change Materials

Riccardo Mazzarello,[1,*] Sebastiano Caravati,[1,2] Stefano Angioletti-Uberti,[2,†] Marco Bernasconi,[2] and Michele Parrinello[1]

[1]*Computational Science, Department of Chemistry and Applied Biosciences, ETH Zurich, USI Campus, via Giuseppe Buffi 13, CH-6900 Lugano, Switzerland*

[2]*Dipartimento di Scienza dei Materiali and CNISM, Università di Milano-Bicocca, Via R. Cozzi 53, I-20125 Milano, Italy*

(Received 8 May 2009; published 24 February 2010)

We computed the Raman spectrum of amorphous GeTe by *ab initio* simulations and empirical bond polarizability models. The calculated spectrum is in very good agreement with experimental data and contains the signatures of all the peculiar local structures of the amorphous phase revealed by recent *ab initio* simulations, namely, tetrahedral Ge and defective octahedral sites for a fraction of Ge (mostly 4-coordinated) and for all Te (mostly 3-coordinated) atoms. In particular, the spectrum above 190 cm^{-1} is dominated by tetrahedral structures, while the most prominent peaks around 120 and 165 cm^{-1} are mainly due to vibrations of atoms in defective octahedral sites. Finally, the peak around 75 cm^{-1}, which dominates the spectrum in *HV* scattering geometry, is mostly due to vibrational modes involving threefold coordinated Te atoms.

DOI: 10.1103/PhysRevLett.104.085503 PACS numbers: 61.43.Bn, 61.43.Dq, 63.50.−x

Phase-change materials (PCMs) based on chalcogenide alloys are of great technological importance due to their ability to undergo reversible and fast transitions between the amorphous and crystalline phases upon heating [1]. This property is exploited in rewritable optical media (CD, DVD, Blu-Ray Disc) and electronic nonvolatile memories (NVM) which are based on the strong optical and electronic contrast between the two phases [1–3].

Although $Ge_2Sb_2Te_5$ (GST) is the most widely studied PCM for applications in NVM, the related binary GeTe compound has also been thoroughly investigated. In spite of this, the structural properties of amorphous GeTe (*a*-GeTe) and GST (*a*-GST) and the mechanisms driving the phase transitions are still debated. A step towards the comprehension of these issues was provided by extended x-ray absorption fine structure (EXAFS) experiments [4,5], which showed that the local structure of GST and GeTe changes upon amorphization. The average coordination of Ge atoms inferred from EXAFS data decreases from sixfold in the crystal to a fourfold tetrahedral coordination of Ge atoms in *a*-GST and *a*-GeTe [4,5]. However, while fourfold coordination can be reliably inferred from EXAFS, bonding angles are subject to large uncertainties. Moreover, this picture is in contrast with the interpretation of other EXAFS data [6] and with reverse Monte Carlo models fitted on x-ray diffraction data [7], which suggest that Ge in *a*-GST and *a*-GeTe keeps an octahedral-like coordination as in the crystal. Recent *ab initio* molecular dynamics (MD) simulations [8,9] of *a*-GST and *a*-GeTe showed that indeed Ge atoms are mostly fourfold coordinated, but only approximately one third of Ge atoms display tetrahedral coordination, whereas the majority of Ge and all Te and Sb atoms are in a defective octahedral environment. These findings have been corroborated by recent core-level spectroscopy experiments [10], which support the presence of two different local environments around Ge.

Signatures of Ge in tetrahedral sites were assigned to specific features of the Raman spectrum of *a*-GeTe prepared by rf-sputtering techniques [11–13]. Different Raman peaks were tentatively assigned [11–13] to vibrational modes of $GeTe_{4-n}Ge_n$ tetrahedra (where $n = 0, \ldots, 4$), but the possible coexistence with octahedral sites was overlooked. Therefore, a compelling experimental identification of tetrahedral Ge has not yet been provided.

In this Letter, we present a calculation of the Raman spectrum of GeTe based on amorphous models generated by quenching from melt within first-principles MD simulations. We will compare the calculated Raman spectrum of melt-quenched *a*-GeTe with the experimental spectrum of *a*-GeTe deposited by sputtering. Although the amorphous phases generated by different means might be slightly different, very similar spectra have been recorded for *a*-GeTe films as-deposited and after several cycles of laser-induced crystallization or amorphization but for the enhancement of a high frequency band (275 cm^{-1}) attributed to Ge segregation [14].

The theoretical spectrum turns out to be in good agreement with experimental data [11,12] and provides a compelling assignment of Raman peaks to specific phonons of the amorphous network. It turns out that, although the main Raman peaks (below 190 cm^{-1}) are mostly due to vibrations of defective octahedra, weaker features at high frequencies (above 190 cm^{-1}) can indeed be assigned to Ge in tetrahedral sites.

To generate a model of *a*-GeTe, we started from a 216-atoms supercell equilibrated in the liquid phase at 1200 K (at the experimental [15] density of *a*-GeTe, 5.95 g/cm^3) by means of the first-principles MD scheme developed by Kühne *et al.* [16] This new method, implemented in the

 © 2010 The American Physical Society

CP2K suite of programs [17,18], was used in our previous simulation of a-GST [8]. Gradient-corrected exchange-correlation functionals [19] and Goedecker pseudopotentials were used [20]. The spin-resolved Kohn-Sham orbitals were expanded in a Gaussian-type basis set of triple-zeta plus polarization quality, whereas the charge density was expanded in plane waves with a cutoff of 100 Ry. The amorphous model was generated by quenching from 1200 to 300 K in 50 ps. The resulting structural and electronic properties are very similar to those reported by Akola and Jones [9]. Details on the structural and electronic properties of our a-GeTe model are given in the supplementary material (see Figs. S1-S6 and Tables I–III in EPAPS [21]). Similarly to previous results on a-GST [8,9], Ge atoms are mostly fourfold coordinated, while Te atoms are mostly threefold coordinated. All Te and 77% of Ge atoms are in a defective octahedral-like geometry with octahedral bonding angles but a lower than six coordination [see inset of Fig. 1(a)]. In the defective octahedral geometry, Ge atoms form three shorter bonds in a $3 + n$ ($n = 0$–2) geometry similar to that of crystalline trigonal GeTe (α-GeTe); see Figs. S3 and S4 in [21]. Some Ge atoms are tetrahedrally coordinated, as inferred from EXAFS data [5], although only in the fraction of 23% (Fig. S5 in [21]). The distribution of different tetrahedral units $GeTe_{4-n}Ge_n$ reported in the inset of Fig. 2(b) shows that the tetrahedral coordination of Ge is favored by homopolar Ge-Ge bonds, as occurs in a-GST [8]. There are no chains of Te atoms but a few dimers (Table II in [21]).

We calculated the phonon density of states (DOS) of a-GeTe (at the supercell Γ point) by diagonalizing the dynamical matrix obtained from the variation of atomic forces due to small atomic displacements (maximum 0.01 Å). The DOS of a-GeTe and its projections on atomic species (Te and Ge in octahedral and tetrahedral sites) are shown in Fig. 1(a). Comparison with the DOS of trigonal α-GeTe is made in Fig. S9 of EPAPS [21]. To quantify the localization properties of the phonons, we report in Fig. 1(b) the inverse participation ratio (IPR) defined for the jth phonon by $\mathrm{IPR} = \sum_\kappa |\frac{\mathbf{e}(j,\kappa)}{\sqrt{M_\kappa}}|^4$, where $\mathbf{e}(j,\kappa)$ are phonon eigenvectors and κ runs over the N atoms in the unit cell with masses M_κ and $\sum_\kappa |\mathbf{e}(j,\kappa)|^2/M_\kappa = 1$. According to this definition, the value of IPR varies from $1/N$ for a completely delocalized phonon, to one for a mode completely localized on a single atom. Phonons above 190 cm^{-1} are mostly localized on tetrahedral sites

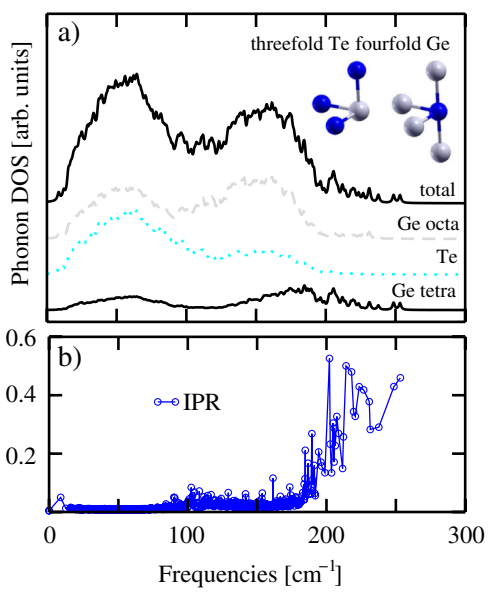

FIG. 1 (color online). (a) Projection of the phonon DOS of a-GeTe on different species [Te, Ge in tetrahedral (tetra) and defective octahedral (octa) sites]. The contribution to the DOS of the jth mode with eigenvector $\mathbf{e}(j,\kappa)$ is multiplied by $\sum_\kappa \frac{|\mathbf{e}(j,\kappa)|^2}{M_\kappa}$, where the sum over κ is restricted to atoms of a given species with mass M_κ. Inset: a sketch of the geometry of defective octahedral sites of 4-coordinated Ge and 3-coordinated Te. (b) Inverse Participation Ratio (IPR) (see text).

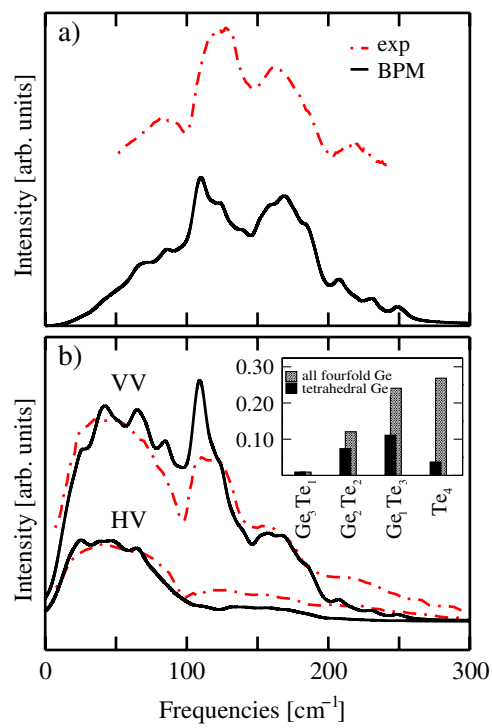

FIG. 2 (color online). (a) Reduced Raman spectrum of the 216-atoms a-GeTe model computed within the BPM for unpolarized light in backscattering geometry (see text) compared with the analogous experimental spectrum from Ref. [11]. The reduced spectrum is obtained by multiplying by $\omega_s^{-4}\omega(n_B + 1)^{-1}$ the Raman scattering (Stokes) cross section given by Eq. (2) in EPAPS [21]. (b) Theoretical and experimental (adapted from Ref. [11]) polarized Raman spectra in HV and VV geometries. The theoretical spectra are obtained by substituting the δ functions in Eq. (2) in EPAPS [21] with Lorentzian functions 5 cm^{-1} wide. We averaged over all possible incident directions of the light [28]. Inset: distribution of $GeTe_{4-n}Ge_n$ polyhedra for fourfold coordinated Ge in the a-GeTe model.

and show up as distinct features in the Raman spectrum, as detailed below.

Since the fully *ab initio* calculation of the Raman spectrum of the 216-atoms model is computationally demanding, we proceeded as follows. First, we generated a small 64-atoms model of *a*-GeTe by quenching from the melt as discussed above. The *ab initio* Raman spectrum in nonresonant conditions of the latter model was computed within density functional perturbation theory (DFPT) [22,23] as discussed, for instance, in our previous work on Sb_2Te_3 [24]. Then a bond polarizability model (BPM) [25] was developed by fitting the *ab initio* Raman spectra of *a*-GeTe (64 atoms) and α-GeTe [26]. Finally, the BPM was used to compute the Raman spectrum in nonresonant conditions of the more realistic 216-atoms model of *a*-GeTe.

Within the BPM, the electronic susceptibility $\underline{\chi}^{\infty}$ is written as a sum of bond polarizabilities α_β as $\alpha_{\beta,ij} = \alpha_{\beta\parallel}\hat{d}_{\beta,i}\hat{d}_{\beta,j} + \alpha_{\beta\perp}(\delta_{ij} - \hat{d}_{\beta,i}\hat{d}_{\beta,j})$, where $\hat{\mathbf{d}}_\beta$ is a unit vector which defines the direction of bond β, whose longitudinal and perpendicular polarizabilities are given by $\alpha_{\beta\parallel}$ and $\alpha_{\beta\perp}$. By assuming that the polarizabilities depend on bond length only, the BPM is defined by the parameter $\alpha_{\beta\parallel} - \alpha_{\beta\perp}$ and the derivatives with respect to the bond length $\alpha'_{\beta\parallel}$ and $\alpha'_{\beta\perp}$ for each type of bond β. To set up a BPM suitable to reproduce the *ab initio* spectra of *a*-GeTe, five types of bonds (Ge(tetra)-Ge(tetra), Ge(tetra)-Ge (octa), Ge(octa)-Ge(octa), Ge(tetra)-Te, and Ge(octa)-Te) were considered. The BPM parameters are fitted on the *ab initio* Raman intensities of the 64-atoms *a*-GeTe model and of α-GeTe [26]. Of course, the BPM for α-GeTe contains Ge(octa)-Te bonds only. Moreover, since the spectrum of the 64-atoms a-GeTe is very weakly dependent on the parameters for the Ge(tetra)-Ge(tetra) bond, those of crystalline Ge [27] have been used.

The Raman spectrum of the 216-atoms *a*-GeTe model computed with the best-fit BPM parameters (Table IV in EPAPS [21]) is compared to the experimental Raman spectrum [11,12] in Fig. 2, which reports both the unpolarized spectrum in backscattering geometry [Fig. 2(a)] and the polarized spectra in *HV* and *VV* geometries [Fig. 2(b)].

The main features of the experimental Raman spectra are well reproduced by theory, in spite of the uncertainties in the empirical BPM. The (slight) misfit in the relative intensities of the peaks might be due to the fact that (a) as opposed to experiments, our spectrum is computed in nonresonant conditions and (b) the limited statistics due to the still small size of the simulation cell might weight differently the contributions from different local structures, as discussed below. The weak features in the range 60–80 cm^{-1} correspond to the broad experimental peak at 75 cm^{-1} (resolved in two Gaussian peaks at 65 and 88 cm^{-1} and assigned to A_1 vibrations of $GeTe_{4-n}Ge_n$ tetrahedra in Ref. [12]). The two main theoretical peaks at 110 and 175 cm^{-1} correspond to the two main experimental peaks at 120 and 165 cm^{-1} (each resolved in two Gaussian and assigned, respectively, to bending modes of corner and edge-sharing tetrahedra in Ref. [12]). The assignments which emerge from the theoretical calculations are different in many respects from the tentative assignments in Ref. [12], which were based on the assumption that the amorphous network consisted only of $GeTe_{4-n}Ge_n$ tetrahedra. Insight on the phonons responsible for the different Raman peaks is gained from the analysis of the reduced Raman spectra projected on tetrahedra and different type of atoms reported in Fig. 3.

It is clear (Fig. 3) that vibrations of tetrahedra dominate the Raman spectrum above 190 cm^{-1}, in form of antisymmetric stretching modes. Stretching of Ge-Ge bonds in tetrahedra mostly contribute to the spectrum above 220 cm^{-1}, and the larger the number of homopolar Ge-Ge bonds in the tetrahedron, the higher is the frequency of the corresponding phonons (Figs. S13 and S14a in [21]). By changing the distribution of the $GeTe_{4-n}Ge_n$ tetrahedra, the Raman features above 220 cm^{-1} change in intensity and frequency, as demonstrated by the comparison of the Raman spectrum of Fig. 2 with that of a second 216-atoms model generated by a fast (20 ps) quenching from the melt (Fig. S11 in [21]). The frequency shift is due to inhomogeneous broadening generated by the different environments of the tetrahedra. We can thus ascribe the discrepancies between the experimental and theoretical

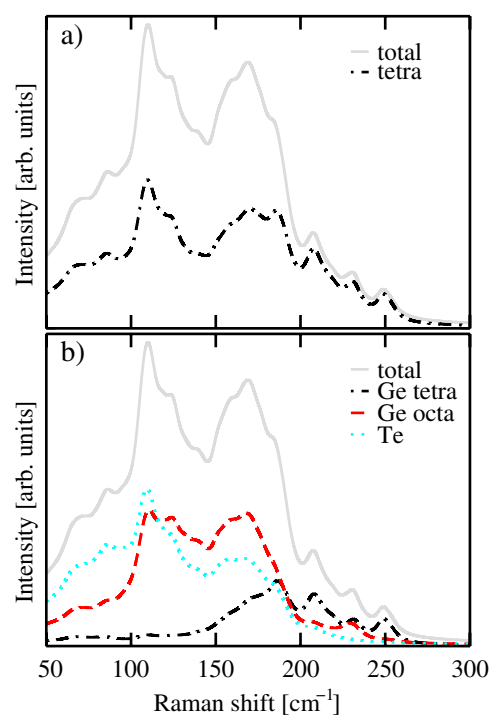

FIG. 3 (color online). Projection of the reduced Raman spectrum in Fig. 2 on (a) all atoms belonging to $GeTe_{4-n}Ge_n$ tetrahedra and (b) tetrahedral Ge, octahedral Ge and Te atoms.

Raman spectra above 200 cm^{-1} to the limited statistics of the tetrahedra distribution.

The projected spectra (Fig. 3) reveal that the features of the Raman spectra at 110 and 175 cm^{-1} are mainly due to vibrations of atoms in defective octahedral environments and not to corner- and edge-sharing tetrahedra, as proposed in Ref. [12] (Fig. S13 and Table III in [21] for the distribution of different types of isolated, corner- and edge-sharing $GeTe_{4-n}Ge_n$ tetrahedra). Although in the topology of a-GeTe one can recognize $TeGe_3$ units typical of α-GeTe and analogous units made of $GeTe_{3-n}Ge_n (n = 0-2)$ plus 1-2 longer bonds, the disalignment of four-membered rings in a-GeTe prevents a classification of normal modes in bending and stretching modes of the pyramidal units such as the E and A_1 modes of α-GeTe [26]. Nevertheless, the projection of the Raman spectrum on bending- and stretching-like displacements of Ge and Te atoms in $TeGe_3$ and $GeTe_{3-n}Ge_n$ units reported in Fig. S16 in EPAPS [21] shows a marginal predominance of stretching-like (bending-like) vibrations in the Raman peak at 175 cm^{-1} (110 cm^{-1}).

Finally, the peaks below 100 cm^{-1} are mostly due to Te atoms threefold coordinated (Fig. 3(b) and Fig. S14c in EPAPS [21]). The C_3-like symmetry of these latter sites [cf. Inset of Fig. 1(a)] gives rise to a Raman tensor with only off-diagonal components, which mostly contributes to the HV polarization, in agreement with the experimental findings [Fig. 2(b)].

In conclusion, based on *ab initio* calculations, we have provided an assignment of the Raman spectrum of a-GeTe to vibrations of specific local structures in the amorphous network which, by comparison with experimental Raman spectra, yields a compelling evidence of the existence of both tetrahedral and defective octahedral structures in a-GeTe.

We thankfully acknowledge the computational resources by the DEISA Consortium under project PHASEMAT, by the Barcelona Supercomputing Center, by CSCS (Manno, CH), and by INFM-CNR-CNISM parallel computing initiative at CINECA. Discussions with R. Bez, M. Ceriotti, A. Modelli, A. Pirovano, and E. Varesi are gratefully acknowledged.

*Corresponding author. Present address: RWTH Aachen University, Aachen, Germany; riccardo.mazzarello@phys.chem.ethz.ch

†Present address: Imperial College, London, UK

[1] M. Wuttig and N. Yamada, Nature Mater. **6**, 824 (2007).
[2] A. Pirovano *et al.*, IEEE Trans. Electron Devices **51**, 452 (2004).
[3] A. L. Lacaita and D. J. Wouters, Phys. Status Solidi A **205**, 2281 (2008).
[4] A. V. Kolobov *et al.*, Nature Mater. **3**, 703 (2004).
[5] A. V. Kolobov, P. Fons, and J. Tominaga, Appl. Phys. Lett. **82**, 382 (2003).
[6] D. A. Baker *et al.*, Phys. Rev. Lett. **96**, 255501 (2006).
[7] S. Kohara *et al.*, Appl. Phys. Lett. **89**, 201910 (2006).
[8] S. Caravati *et al.*, Appl. Phys. Lett. **91**, 171906 (2007).
[9] J. Akola and R. O. Jones, Phys. Rev. B **76**, 235201 (2007); Phys. Rev. Lett. **100**, 205502 (2008).
[10] A. Klein *et al.*, Phys. Rev. Lett. **100**, 016402 (2008).
[11] K. S. Andrikopoulos *et al.*, J. Phys. Chem. Solids **68**, 1074 (2007).
[12] K. S. Andrikopoulos *et al.*, J. Phys. Condens. Matter **18**, 965 (2006).
[13] R. De Bastiani *et al.*, Phys. Rev. B **80**, 245205 (2009).
[14] O. Salicio *et al.*, J. Appl. Phys. **105**, 033520 (2009).
[15] W. K. Njoroge, H. W. Woltgens, and M. Wuttig, J. Vac. Sci. Technol. A **20**, 230 (2002).
[16] T. D. Kühne *et al.*, Phys. Rev. Lett. **98**, 066401 (2007).
[17] M. Krack and M. Parrinello, in *High Performance Computing in Chemistry*, edited by J. Grotendorst (NIC, Jülich, 2004), Vol. 25, pp. 29, http://cp2k.berlios.de.
[18] J. VandeVondele *et al.*, Comput. Phys. Commun. **167**, 103 (2005).
[19] J. P. Perdew, K. Burke, and M. Ernzerhof, Phys. Rev. Lett. **77**, 3865 (1996).
[20] S. Goedecker, M. Teter, and J. Hutter, Phys. Rev. B **54**, 1703 (1996).
[21] See supplementary material at http://link.aps.org/supplemental/10.1103/PhysRevLett.104.085503 for additional data on structural, electronic, and vibrational properties of our a-GeTe models.
[22] S. Baroni *et al.*, Rev. Mod. Phys. **73**, 515 (2001).
[23] P. Giannozzi *et al.*, J. Phys. Condens. Matter **21**, 395502 (2009); http://www.quantum-espresso.org.
[24] G. C. Sosso, S. Caravati, and M. Bernasconi, J. Phys. Condens. Matter **21**, 095410 (2009).
[25] M. V. Wolkenstein, C. R. Acad. Sci. URSS **30**, 791 (1941); M. A. Eliashevich and M. V. Wolkenstein, J. Phys. (USSR) **9**, 101 (1944).
[26] The E and A_1 Raman active modes of trigonal GeTe obtained within DFTP (see EPAPS [21]) are at 90 cm^{-1} and 152 cm^{-1}, which compare well with the experimental values of 98 and 140 cm^{-1} [E. F. Steigmeier and G. Harbeke, Solid State Commun. **8**, 1275 (1970)].
[27] S. Go, H. Bilz, and M. Cardona, Phys. Rev. Lett. **34**, 580 (1975).
[28] The total Raman cross section for unpolarized light in backscattering geometry averaged over all possible incident directions is computed from Eq. (7) of Ref. [24], with the substitution $4(R_{xx}^2 + R_{yy}^2 + R_{zz}^2) + 7(R_{xy}^2 + R_{xz}^2 + R_{yz}^2) + (R_{xx}R_{yy} + R_{xx}R_{zz} + R_{zz}R_{yy}) \rightarrow 30|\mathbf{e}_S \cdot \mathbf{R}^j \cdot \mathbf{e}_L|^2$. See EPAPS [21] for the corresponding formulas for polarized HV and VV spectra.